Electrospinning Fabrication, Structural Analysis, Thermomechanical, Lyophobic, and Biocompatible Properties of Cottonseed Protein Isolate/Poly(ethylene oxide) Composite Fiber Mats

Electrospinning fabrication, structural analysis, thermo-mechanical, lyophobic and biocompatible properties of cottonseed protein isolate/polyethylene oxide composite fiber mats

Yanli Jiang,[1] Qiqi Wu,[1] Yuru Zheng,[1] Juan P. Fernández-Blázquez,[3] Francisca Martinez-Hergueta,[4] James H. Clark[5], Jianwei Guo,[1,2] and Hangbo Yue,*[1,2]

[1] Guangdong Provincial Key Laboratory of Plant Resources Biorefinery, School of Chemical Engineering & Light Industry, Guangdong University of Technology, Guangzhou 510006, China.

[2] Jieyang Branch of Chemistry and Chemical Engineering Guangdong Laboratory(Rongjiang Laboratory), Jieyang 515200, China

[3] IMDEA Materials Institute, Eric Kandel 2, Getafe, Madrid 28906, Spain.

[4] School of Engineering, Institute for Infrastructure and Environment, The University of Edinburgh, William Rankine Building, Edinburgh, UK.

[5] Circa Renewable Chemistry Institute, Green Chemistry Centre of Excellence, University of York, York, UK.

*Correspondence: *E-mail:hangbo.yue@gdut.edu.cn (H.Y).*

A Table of Contents (TOC) graphic

"For Table of Contents use only".

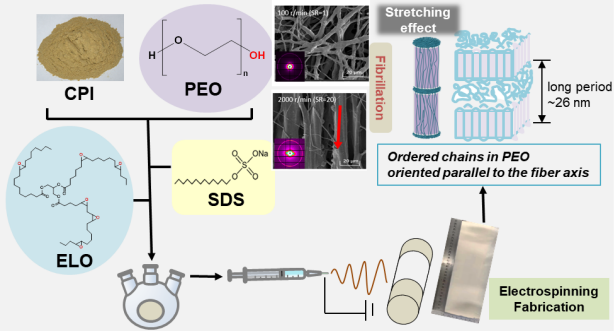

Abstract: Macroscopic, robust, lyophobic, and biocompatible protein fiber mats derived from cottonseed protein isolate (CPI) as a renewable feedstock were successfully fabricated by electrospinning, with incorporation of polyethylene oxide (PEO) for fiber spinnability improvement. Influences of spinning solution concentration, CPI:PEO ratio, fiber collecting velocity and epoxidized linseed oil (ELO) content on the fiber mat properties were investigated. The fiber mats collected at high speeds showed clear increases of tensile strength and stiffness, which was largely due to the stretching effect on favoring polymer chain alignment, crystal orientation, and protein secondary structure ordering, as revealed by SAXS/WAXS and ATR-FTIR peak deconvolution analysis. In addition, the mechanical properties and thermal stability of the fiber mat can be further improved using ELO as a green crosslinking agent. Furthermore, the CPI/PEO fiber mats show excellent solvent resistance, reduced surface free energy, low water vapor permeability and superior biocompatibility. The reported fiber mats hold great potential in biomedical dressing, air filtration and biodegradable packaging applications.

1 Introduction

Nowadays, it is urgent to reduce the consumption of non-renewable fossil resources such as oil, coal and natural gas, because their use rate is much higher than that of natural geological processes, which makes their use unsustainable in the long run. In addition, the use of fossil resources is producing carbon dioxide at a rate that the natural environment cannot assimilate, leading to increased levels of carbon dioxide in the atmosphere, which is often considered to be a direct cause of climate change. By contrast, switching to renewable biomass as a feedstock can alleviate the burden of carbon emissions[1]. Existing products might be replaced with alternatives that are inherently safer and reduce the environmental footprints, such as biocompatible and biodegradable plastics[2]. Among the naturally renewable raw materials, protein has received widespread attention because of the characteristics of its low cost, wide sources, biodegradability, and can be extracted from plant resources by multiple ways. More importantly, proteins are composed of various amino acids, suggesting versatile chemical reactivity. Furthermore, they can be processed into biodegradable polymeric materials by existing processing approaches for polymer materials.[3, 4] In recent years, environmentally friendly protein-based materials have been widely reported, such as bioplastics[5], bioadhesives[6], biofibers[7] and packaging films.[8]

According to the United States Department of Agriculture, worldwide oil seed production reached 644 million metric tons in 2022, of which about 7% were cottonseed, representing the next most important source of plant proteins after soybean (61%) and rapeseed (13%).[9] For every 100 pounds of cotton harvested approximately 30 pounds of cottonseed meal remains after extracting the oil. The meal, which has around 50% cottonseed protein (CP), is mainly used as an animal feed[10]. With the price of cotton continuing to decline, the development of higher value products from cottonseed protein would provide an economic boost to cotton producers and

processors.[11] However, only limited research has been carried out using the proteinaceous by-products from either glanded or glandless cotton to fabricate value-added products, such as protein-derived films/plastics[12, 13] or adhesives[14] used for plywood bonding[15]. Cottonseed protein isolate (CPI) has been reported to be comparable to or better than soybean protein isolate with respect to adhesion performance[16] and water resistance[17]. Nevertheless, the processability of protein-based nanofibers using protein alone is quite challenging.[18] For example, protein molecular chains are difficult to be stretched into continuous nanofibers by electrospinning because of their globular structure commonly encountered in most proteins, low purity, low viscosity of their processing solutions, and short molecular chains that often leads to a lack of intermolecular entanglements[19]. Another limitation in electrospinning process is that when the protein is dissolved in the solvent, the formation of macromolecular ionomeric structure might make surface charge density in the solution too high and causing repulsion problems. One feasible solution is the addition of non-ionogenic polymers with flexible chains into the protein spinning solution. As a result, physical entanglements between polymer chains and protein macromolecular chains[19], and their chemical interactions[20], can increase the viscosity or reduce the conductivity of the spinning solution, eventually improving the spinnability[21]. Successful examples of electrospinning fiber mats derived from soy protein have been reported using poly β-hydroxybutyrate dissolved in formic acid, as an efficient way of improving the processability of protein-based nanofibers[22]. Efforts have also been made to increase the chemical/physical stabilization of soy protein fiber mats, e.g. by a photo-crosslinking strategy[23].

In addition to processability, the mechanical properties, solvent resistance, and biocompatibility of protein-based nanofibers are critical to a variety of applications. Chemical crosslinking is often applied to improve the breaking strength and hydrophobicity of protein

fibers. For instance, 1-ethyl-3-(3-dimethyl-aminopropyl) carbodiimide hydrochloride, was used to crosslink recombinant human collagen/chitosan nanofibers, and the composite fibers showed better performance in terms of elongation at break (over 70% improvement) and Young's modulus (over 200% improvement).[24] Epoxidized linseed oil (ELO) shows high reactivity due to the presence of epoxy functional groups, and thus can be incorporated into proteinaceous matrix as a cross-linking agent.[25] For example, keratin based materials cross-linked by a combination of ELO and dodecenylsuccinic anhydride displayed good thermomechanical properties and water resistance.[26] Moreover, increasing the percentage of proteins in the electrospun fiber solution has been proven to increase cell viability of the resulting fiber scaffold[27]. In this regard, plant protein isolate used in this study for fiber mat fabrication is expected to provide desirable biocompatibility.

The objective of this work is to evaluate and process cottonseed protein waste into high value-added fiber mat materials with superior mechanical, lyophobic and biocompatible properties. Firstly, cottonseed protein isolate (CPI with protein content >90%) was obtained by dialysis after alkali dissolution and acid precipitation of raw CP waste. Impurities in the CP waste (like ash, carbohydrates, cotton fiber and gossypol[28]) were removed, purifying the raw proteins and thus contributing to the stable formation of the protein fiber. Secondly, fiber spinnability of the CPI spinning solution was significantly improved after blending the modified CPI with PEO in water. Macroscopic CPI/PEO composite fiber mats were successfully fabricated by electrospinning, and fibers with various orientation degrees can be collected by changing the rotating speed of the fiber collector. Thirdly, epoxidized linseed oil used as a green crosslinking agent can further improve applicable properties of the fiber mat. Overall, the newly electrospun fiber mats with excellent biocompatible, lyophobic and mechanical properties, using conttonseed waste as a

sustainable feedstock are likely to be suitable for various applications like biomedical dressing, air filtration and biodegradable packaging.

2 Experimental

Reagents and materials

Hydrochloric acid, sodium oxide, sodium dodecyl sulfate (SDS) and ethanol were purchased from Tianjin Damao Chemical Reagent Factory (China). Poly(ethylene oxide), PEO with a molecular weight of 600,000 g/mol were bought from Shanghai Macklin Biochemical CO., Ltd. (China). All reagents were used without further purification unless stated otherwise. Cottonseed protein powder was purchased from Qingdao Kerui Culture Medium Co., Ltd. (China). Epoxidized linseed oil (ELO EPOXOL®9-5) was obtained from Zhejiang Xingbang Polymer Material Co., Ltd. (China). Detailed treatments and evaluation of the cottonseed protein are provided in the Supporting Information (Section S1, Supporting Information).

Preparation of spinning solution

The electrospinning solution was a mixture of CPI and PEO solution. The CPI solution was obtained by dissolving it in distilled water with slow-drop of 1 $mol \cdot L^{-1}$ NaOH solution and continuously stirring for 5 h at room temperature. The PEO solution was prepared by directly dissolving it in distilled water with continuously stirring at 60 °C for 12 h. A small amount (1wt%) of SDS was also added into the mixture. A series of the spinning solution at different concentrations, i.e., total amount of CPI and PEO in water of 8, 10, 12, 14, 16 wt%, were obtained, keeping a constant CPI:PEO ratio of 2:8. Afterwards, while maintaining the CPI:PEO concentration at 12 wt%, another series of

the spinning solution with varied CPI:PEO ratio (1:9, 2:8, 3:7, 4:6) were also prepared. For crosslinked samples, 10, 20, 30% ELO (relative to CPI content) were added respectively to the mixture at 14 wt% with CPI:PEO = 2:8. The composition and nomenclature of the spinning solution are listed in Table 1.

Table 1 Nomenclature and composition of electrospinning solutions

Samples	Solution concentration(wt%)	w(CPI) (g)	w(PEO) (g)	w(CPI):w(PEO)	SDS(wt%)	ELO (wt%, relative to CPI)
CPI/PEO-8	8	0.8	3.2	2:8	1	
CPI/PEO-10	10	1	4	2:8	1	
CPI/PEO-12	12	1.2	4.8	2:8	1	
CPI/PEO-14	14	1.4	5.6	2:8	1	
CPI/PEO-16	16	1.6	6.4	2:8	1	
CPI/PEO-10/90	12	0.6	5.4	1:9	1	
CPI/PEO-20/80	12	1.2	4.8	2:8	1	
CPI/PEO-30/70	12	1.8	4.2	3:7	1	
CPI/PEO-40/60	12	2.4	3.6	4:6	1	
CPI/PEO/ELO-0	14	1.4	5.6	2:8	1	0
CPI/PEO/ELO-10	14	1.4	5.6	2:8	1	10
CPI/PEO/ELO-20	14	1.4	5.6	2:8	1	20
CPI/PEO/ELO-30	14	1.4	5.6	2:8	1	30

Fabrication of CPI/PEO composite fiber

All fibers were prepared at 30 °C and 30% relative humidity (RH) using an electrospinning machine (ET-3556H, Beijing Yongkang Leye Technology Development Co. Ltd., China) with an applied voltage of 15-20 kV, a needle-to-collector distance of 15 cm, and a flow rate of 2 mL/h. Each spinning solution was loaded into a 10 mL syringe with a 22-gauge blunt-tipped needle. A rotating mandrel wrapped with an aluminum foil was used as fiber

collector. Macroscopic fiber mat samples with desired thickness for various measurements were collected after around 5h electrospinning, then dried in vaccum at 60 °C for 2h (post curing), and stored in a desiccator prior to use. Fibers were collected at four rotating speeds (100, 500, 1000, and 2000 rpm) to evaluate the effect of stretching and fiber orientation on fiber mat morphology and properties. For better interpretation of the stretching effect, the collecting speed of 100 r/min was denoted as the reference of Stretching Ratio (SR=1), 500 r/min as SR=5, 1000 r/min SR=10, and 2000 r/min as SR=20.

Characterization

Fourier transform infrared spectroscopy (FTIR) was conducted using a Nicolet 380 FTIR spectrometer, and the spectra of samples with KBr pellets were collected in the region of 4000-400 cm^{-1} and averaged over 16 scans. For fiber mat sample inspection, a spectrometer (Nicolet iN10) with attenuated total reflectance (ATR) accessory was used; the ATR-FTIR spectra were collected after 32 accumulated scans at 4 cm^{-1}.

2D wide-angle X-ray diffractograms of fiber mat samples (25 mm ×7 mm × 0.12 mm) were recorded on Hypix-6000 detector (HomeLab, Rigaku) with a resolution of 100 μm × 100 μm, Cu Kα radiation, λ = 1.54 Å. The beam centre and sample to detector distance (71.3mm) was calibrated using a silicon crystal standard.

The synchrotron radiation small-angle X-ray scattering (SAXS) experiments were performed at beamline (BL16B) at the Shanghai Synchrotron Radiation Facility (SSRF) using high energy X-ray (10 keV) with a wavelength of 1.24 Å. 2D patterns were captured by a Pilatus 2M X-ray detector at a distance of 1 m from the sample, with an exposure time of 20 s. Air scattering correction and image integration of SAXS patterns

were processed by the software package FIT 2D[29]. The Bragg's long period (L_B) quantifying the average periodicity of lamellar structure is viewed as the sum of average thickness of lamellae and inter-lamellar amorphous polymer region. In practice, the value of L_B can be estimated by the peak position at maximum scattering vector (q_{max}) in SAXS profile with Lorentz correction[30], as shown in Equation (1).

$$L_B = \frac{2\pi}{q_{max}} \quad (1)$$

$$q_{max} = \frac{4\pi \sin\theta}{\lambda} \quad (2)$$

Scanning electron microscopy (SEM) was performed using a field-emission Inspectors TESCAN MIRA LMS to observe the microscopic morphology of the material. Before collecting SEM images, samples were coated with a thin gold layer using Oxford Quorum SC7620 at 10 mA.

X-ray Photoelectron Spectrometer, XPS (Thermo Scientific K-Alpha XP) was used to analyse the atomic composition and valence state. Samples were exposed to an X-ray source (beam spot 400 μm) at 12 kV and 6 mA. C1s binding energy of 284.8eV (C-C bond) was used as the reference standard.

Nitrogen isothermal adsorption-desorption experiments were conducted on a BSD-PM analyzer. Prior to the measurement, samples (600-700 mg) were degassed at 100 ºC in vacuum for 300 min. Brunauer–Emmett–Teller (BET) specific surface area (S_{BET}) was obtained by applying BET multi-point method in a P/P0 range from 0.01 to 0.1, total pore volume calculated from isotherm at P/P_0=0.99, and average pore size estimated from the Barrett-Joyner-Halenda (BJH) method.

The cross-linking extent/degree was investigated according to the following method previously reported[31]. Briefly, 10 mg of the fiber mat sample was placed into a solution,

which contains a mixture of 1 mL 0.01% 2,4,6-trinitrobenzene sulfonic acid (TNBS) and 1 mL 4% sodium hydrogen carbonate. The mixture was heated at 40 °C for 2 h, followed by a hydrolysis process by an addition of 2 mL 6 N HCl at 60 °C for 1.5 h. The absorbance of solution was measured by UV-vis spectroscopy at a wavelength of 246 nm (peak absorbance). The degree/extent of cross-linking extent (%) was calculated by (1 - Absorbance of cross-linked sample / Absorbance of non-cross-linked sample) × 100.

Property measurements

Tensile mechanical properties were measured by a universal testing machine (Inspekt Table Blue 5 KN, H&P Germany). Fiber mat samples of approximately 1.5 mm thickness and 40 x 20 mm^2 dimensions were placed on a paper cardboard frame prior to tensile test, see details in our previous study[32]. Tensile tests were conducted under position control at a cross-head displacement rate of 10 mm/min and a gauge length of 20 mm. 6 repetitions were conducted for each configuration and the average and standard deviation values were reported.

Contact angles and surface energy were determined by optical contact angle instrument (OCA100, DataPhysics) using varied probing liquids including water, ethylene glycol, glycerol, diiodomethane. In a typical experiment, a small droplet (1 μL) was brought to contact with the sample surface, followed by static contact angle measurements at six different surface locations for each sample, and an averaged value was reported.

The rheological properties were obtained by loading the spinning solution of specified volume into the pressure vessel on the PP25 flat rotor rotating platform of a rheometer (MCR301, Anton Paar) at room temperature with a shear rate of 0.1-60 s^{-1}. For

assessment of cross-linking effect, dynamic viscosities were recorded with a shear rate of 10 s^{-1}.

Thermogravimetric analysis (TGA) experiments were performed with a thermogravimetric analyzer (NETZSCH STA 409 PC) by heating samples in a nitrogen atmosphere with a flow rate of 20 mL min^{-1}, at a rate of 10 ºC/min from room temperature to 600 ºC. Differential scanning calorimetry (DSC) analysis was performed on a DSC analyzer (DSC 3+, Mettler-Toledo) equipped with a cooling accessory and nitrogen atmosphere at a flow rate of 50 mL min^{-1}. A standard run sequence of heating–cooling–heating was used to remove the heating history. The heat flows from -90 ºC to 160 ºC were recorded as a function of temperature. For isothermal analysis, samples were heated to 100 ºC for 3 min with a heating rate of 10 ºC/min, then cool down to a temperature of 52 ºC (best for PEO crystallization) maintaining for 30 min, followed by a heating run to 100 ºC again at a rate of 10 ºC/min.

Water vapour permeability (WVP) was tested using a commercial WVP tester (W3/030, Labthink Ltd., China) at a humidity of 89%RH. Prior to measurements, the composite fiber mat was cut into a disc shape with a diameter of 3 cm and preheated at 37.7 ºC for 4h. Each sample was measured three times to ensure the repeatability of the measurements.

Biocompatibility of the composite fiber mat was evaluated by the cell counting kit 8 (CCK-8) method using mouse skin fibroblast cells (L929). 6000 cells were seeded in a 96-well plate with 100 μL/well, and the plates were incubated in a humidified incubator (37 ºC, 5% CO_2) to allow cells to adhere to the well walls. The liquid extract of samples at 200 mg/L and the cell culture solution (10% CCK-8 solution) was soaked in the cell

growth medium for 2 h. Finally, each well's absorbance at 450 nm was measured on a microplate reader. Each group was tested three times in parallel, and cell viability (%) can be calculated by Equation (3).

$$Cell\ viability = \frac{A_{\text{sample}} - A_{\text{blank}}}{A_{\text{control}} - A_{\text{blank}}} \times 100\% \quad (3)$$

where A_{sample}, A_{blank}, and A_{control} are the absorbance value of the fiber sample, the blank (no sample), and the control (deionized water), respectively.

3 Results and discussion

Electrospinning fabrication of CPI/PEO composite fiber mat

Cottonseed protein powder with 50% protein content was concentrated by an alkali solution and acid precipitation, followed by a dialysis treatment, giving rise to cottonseed protein isolate with > 90% protein content, see details in Supporting Information (Section S1). The positions of characteristic peaks in the FTIR spectra (Figure S1, Supporting Information) are the same between CP and CPI, suggesting that the purification treatment has negligible impact on chemical functional groups of cottonseed protein. The SDS-PAGE image (Figure 1a) indicates that molecular weight of the CPI is in the range of 10-60 kDa, consisting of globulin protein fractions[33], i.e., 11S (glycinin) fraction with molecular weights of 20-35 kDa, 2S (conglycin) fraction of 8-20 kDa, and 7S (β-conglycinin, majority) fraction of 42-57 kDa[34]. The purified protein was denatured by adding 1 wt% sodium lauryl sulfate (SDS) to relax peptide chains folded, and then blended with high molecular weight polyethylene oxide (PEO, 600,000 g/mol) in water, giving rise to the fiber spinning solution for electrospinning fabrication, see Figure 1c.

Different concentrations (8, 10, 12, 14, and 16wt%) of the spinning solution were achieved by changing the total amount of the CPI and PEO.

The spinning solution without SDS was unstable resulting in liquid droplets instead of the typical Taylor cone necessary to form macroscopic electrospun nanofibers. The incorporation of SDS surfactant to the CPI/PEO spinning solution results in an elevation in ion concentration, which in turn increases the electrical conductivity of the solution[35]. On the other hand, the surfactant can reduce the surface tension of the spinning solution and further increase its viscosity by forming micelle complexes with soluble polymers[36], thereby promoting the formation or spinnability of nanofibers[37]. In Figure 1b, the apparent viscosity of the spinning solution increased significantly under shear forces with the increase of solution concentration, from 3.83 Pa·s (10 wt%) to 61.78 Pa·s (16wt%). High viscosity of the spinning solution was unfavourable, as entangled polymer chains would easily block the needle tip. The apparent viscosity curves were fitted with the empirical power law model[38]:

$$\log (\text{viscosity}) = \log K' + (n - 1) \log (\text{shear rate}) \quad (4)$$

where K' is the flow consistency index (Pa·s) indicating the resistance to change of material shape, and n is the flow behaviour index. If $n = 1$, the fluid has Newtonian behaviour, while $n < 1$ indicates a pseudoplastic (shear-thinning) behaviour. With the increase of spinning solution concentration, the flow consistency index K' value increases while the flow behaviour index n decreases (Table S2, Supporting Information), indicating a pseudoplastic behaviour, i.e., shear-thinning effect. These findings are in agreement with the literature, since a higher number of PEO and SPI chains tend to form

more entangled bridge, which are likely to unfold or be broken in a shear-flow field[39]; therefore, a more like shear-thinning behaviour is expected.

Afterwards, macroscopic fiber mats are produced by continuous electrospinning for 5 h (Figure 1d). All fiber mat specimen with dimensions of approximately 1.5 mm thickness and 300 × 200 mm^2 present smooth surfaces (Figure 1e). SEM microscopy reveals a diversity of fiber morphologies as a function of the processing parameters (Figure 1f). An increase in spinning solution concentration results in a gradual increase in the diameter of electrospun fibers. For instance, the average fiber diameter (measured by Image J software) of CPI/PEO-10 is 1.10 ± 0.35 μm, versus 2.88 ± 1.28 μm for CPI/PEO-16. Spindle-shaped fiber beads appear at low concentrations with rough surfaces and branched fine fibers, whilst the fiber surfaces become smoother and more uniform at 14 or 16 wt% concentration. Actually, the centimetre-long fiber mats are composed of micro- and nano-fibers that are intertwined and condensed together (see membrane-like mat in Figure 1e). Since as-spun fibers are connected closely with one another, the macroscopic fiber mats have limited pore volume (~0.001 ml/g) with low BET surface area (< 1 m^2/g), as shown in Supporting Information (Figure S2 BET multi-point method and Figure S3 BJH-desorption pore size & pore volume analysis). Interestingly, the average size of pores (BJH) between fiber bundles increased with the increase of spinning solution concentration, i.e., from 8.5 nm (CPI/PEO-10), 8.7 nm (CPI/PEO-12), to 15.3 nm (CPI/PEO-14) and 14.4 nm (CPI/PEO-16).

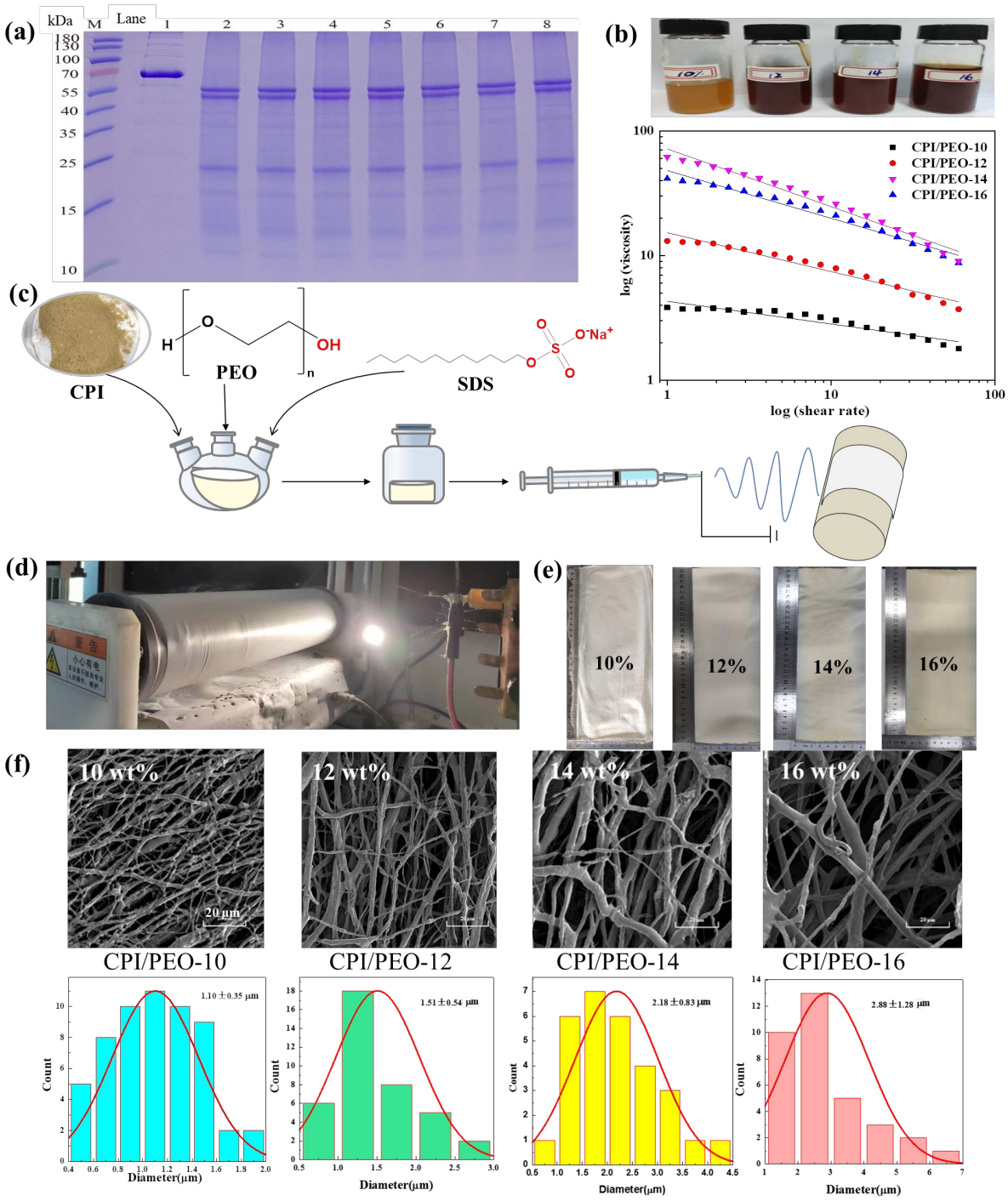

Figure 1. Fabrication of the fiber mat. (a) The Coomassie Brilliant Blue R250 stained SDS-PAGE for cottonseed protein isolate. M (Marker): standard protein ladder; Lanes 1: bovine serum albumin; 2-8: same CPI in Tris - HCl buffer. (b) The rheological flow curves converted to the power law model, together with photos of spinning solution. (c) Schematic representation of

electrospinning technique. Chemical structures of PEO and SDS are included for clarity. (d) Electrospinning set-up. (e) Photos of the electrospun fiber mats. (f) SEM images along with fiber diameter distribution.

Chemical structure analysis

Structural information and chemical interactions between CPI, PEO and the crosslinker ELO in the composite fibers were analyzed by FTIR and XPS spectroscopy, as shown in Figure 2. IR adsorption peaks of the CPI/PEO composite fiber are the superposition of the characteristic peaks of CPI and PEO (Figure 2a,b), regardless of the spinning solution concentration (10, 12, 14, 16wt%) and CPI:PEO ratio (1:9, 2:8, 3:7, 4:6). Specifically, characteristic IR signals of cottonseed protein include N-H and O-H stretching vibrations (ca. 3380 cm^{-1}), as well as C=O stretching in amide I (1657 cm^{-1}), and N-H bending and C-N stretching in amide II (1540 cm^{-1}). As for PEO, C-H stretching vibrations appear at 2875 cm^{-1}; triple peaks at 1148 cm^{-1}, 1100 cm^{-1}, 1057 cm^{-1} correspond to symmetric and asymmetric vibration of C-O-C; characteristic peaks at 843 cm^{-1} and 960 $cm^{-1}$are ascribed to the formation of C-H helical conformation[40]. A tiny new peak appeared at 3290 cm^{-1} characteristic of the hydrogen-bond related signal between CPI and PEO macromolecules. A similar study in the literature found interactions between whey protein and PEO increase chain entanglements[41], thus greatly improving protein spinnability, which is aligned with our findings, pointing at the impossibility to electrospinning of pure CPI into nanofibers.

To further investigate the effects of the PEO blending treatment, the protein secondary-structural components on the Amide I bands were determined using deconvolution[42], and curve fitting of FTIR spectra. The peak deconvolution analysis on the secondary structure

of protein including regularly ordered α-helix and β-sheet forms, and the irregular β-turn form, has long been studied [43], and applied herein to estimate the percentage of the protein secondary structure[44]. Detailed spectral analysis is shown in Fig.2c. Table S3 (Supporting Information) lists the estimated percentages of the three secondary-structural components, α-helix, β-sheet and β-turn. While irregular β-turn form accounts for about 15%, a total of 85% represents the predominantα-helix and β-sheet forms; obviously the CPI:PEO ratio (1:9, 2:8, 3:7, 4:6) has negligible effect on these secondary-structural components. However, when it comes to the β-sheet share alone, a lower amount of PEO seems to favour the ordered β-sheet formation, with the percentage being 26%, 27%, 28% and 30% for CPI/PEO-10/90, 20/80, 30/70 and 40/60, respectively.

In Figure 2d, the cross-linking treatment on the chemical structure of the CPI/PEO fiber was revealed. In detail, the characteristic absorption peaks appear at 823, 847 and 1734 cm^{-1} and are ascribed to the stretching vibration of epoxy and ester carbonyl groups in neat ELO. After adding ELO into CPI/PEO composite fiber, reactions between ELO's epoxy group and amino and carboxylic groups within the protein are highly likely to take place. Indeed, the disappearance of epoxy characteristic signals at 823, 847 cm^{-1} (see enlarged spectra)[45], and gradually increase the intensity of the newly formed ester carbonyl groups (Figure S4, Supporting Information). The absence of peak at 1734 cm^{-1} suggests epoxy groups are consumed after the cross-linking reaction. Furthermore, the intensity of -OH absorption at 3363 cm^{-1} noticeably increased, which is due to the large increase in amount of hydroxyl groups generated from the reaction between epoxy and amino groups (Figure S4, Supporting Information)[46]. Possible chemical interactions were also investigated by XPS analysis and corresponding C1S curves were displayed in

Figure 2e. For the CPI/PEO/ELO-0 control sample, three peak signals resulting from C=O, C-O/C-N, and C-C/C-H bonds can be clearly identified. As a comparison, the CPI/PEO/ELO-20 with 20% ELO addition, the band signal of C-O/C-N was clearly diminished, as its corresponding atomic % decreased from 27.22% to 11.79%, along with C=O atomic % remaining unchanged (8.42% vs. 8.45%). Therefore, the cross-linking reaction prevails among the ELO epoxy group and protein amino groups, in line with the FTIR result. Furthermore, the degree/extent of cross-linking extent (%) of CPI/PEO/ELO mats was estimated by the TNBS method[31], and it came out as 40% for CPI/PEO/ELO-10, 43% for CPI/PEO/ELO-20, and 48% for CPI/PEO/ELO-30.

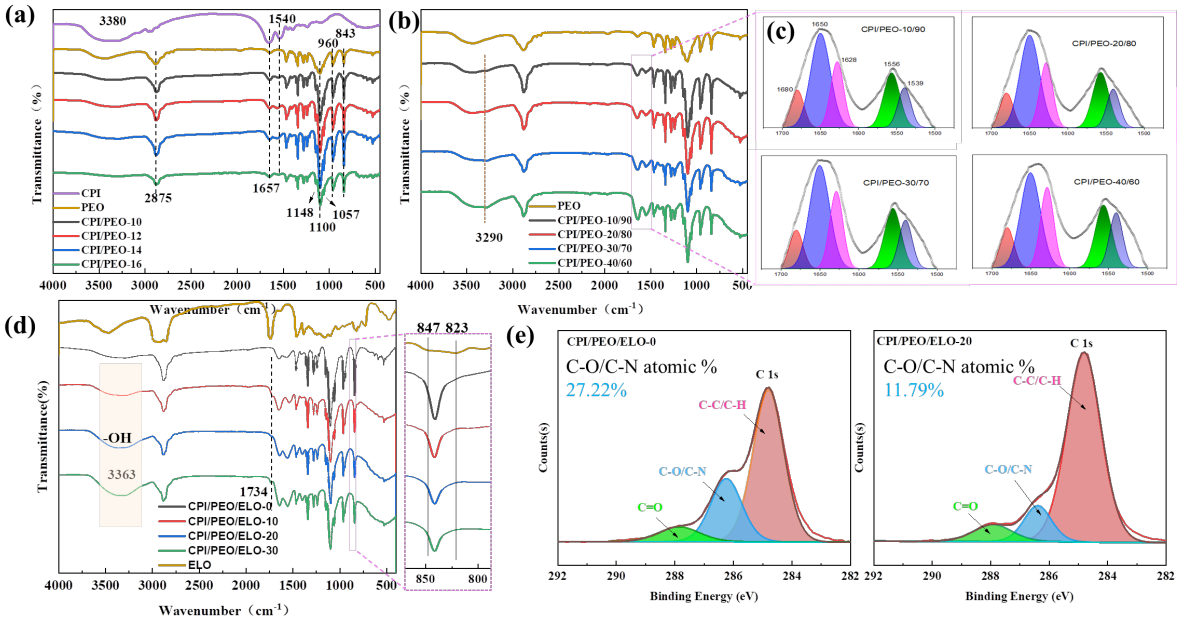

Figure 2. Spectroscopic analysis on the chemical structure of the fiber mat. (a) FTIR spectra of CPI/PEO fiber, neat PEO and CPI for comparison. (b) FTIR spectra of the fiber with different CPI/PEO ratio. (c) The enlarged pink region in (b) with fitting curves of amide I and amide II bands estimating the percentage of protein secondary structure profile. (d) FTIR spectra of the cross-linked fiber with enlarged region between 780 and 870 cm^{-1}, suggesting ring-opening

consumption of ELO epoxy groups. (e) XPS curves of the ELO-crosslinked sample in comparison with CPI/PEO/ELO-0.

The stretching orientation effect

The stretching effects on CPI/PEO fiber morphology and its structure were investigated using fiber mats collected from increasingly rotating speed of the collector, from 100 r/min, denoted as initial stretching ratio, SR=1, through 500 r/min (SR=5), 1000 r/min (SR=10), to 2000 r/min (SR=20). The microscopic morphology of these fibers is shown in Figure 3a. A spider-web like morphology with a randomly distributed fiber orientation was observed at the initial ratio; however, an orderly arrangement of fiber and a preferential fiber alignment is found in mats with higher SR values. Figure S5 (Supporting Information) presents examples of 2D WAXD patterns of the CPI/PEO composite spun-fiber mats at varied fiber collecting roller rates. A transition of the orientation of PEO crystal lattice was observed, from randomly isotropic scattering (SR=1) to oriented non-isotropic scattering (SR=5, SR=10, SR=20), in light of the change from isotropic halo rings to discrete crystalline arcs. However, the stretching ratio has negligible effect on PEO crystal structure (PEO molecules form 7/2 helical conformation and crystallize in a four-chain monoclinic unit cell[47]), as peak positions of main reflections[48], (120) plane at 19.1°, (032)/(112)at 23.2° remain unaltered, see radial profiles in Figure 3b. Azimuthal projection plots covering the major two PEO reflections (Figure 3c) also reveal that the fiber mats fabricated at 100 r/min presented an isotropic fiber orientation distribution function, and that the mats produced at 2000 r/min present highly oriented fiber alignment towards the spinning direction, with concentrated diffractions appearing near equator direction.

Figure 3d shows synchrotron 2D SAXS patterns together with their 1D integrated diffractograms, and illustrates the stretching effect on fiber orientation. From 2D SAXS patterns, an isotropic diffuse pattern near the beam stop was observed for the randomly oriented fiber mat (SR=1), which is ascribed to the scattering from nanofibers in all directions. Aligned fiber mats (SR=5, 10, 20), however, displayed an elliptical shape in this region with the main axis in equator direction, thus indicating an elongated fibrillar structure that was also seen in other aligned electrospun polymer fibers[49]. With increasing stretching ratio, less scattering elements within a given volume of fiber mat are expected, resulting in decreased intensity over wide q range (0.3~1.8 nm^{-1}), see 1D integrated plots. Moreover, the peak (at around 1.6 nm^{-1}, shaded area) is ascribed to ordering configuration of bio-macromolecular chains at broader range. The scattering peak at d-spacing distance of ~3.9 nm among these ordered chains is unsurprising as regular β-sheets of protein polypeptide hold similar ordering distances[50], like those in silk protein[51].

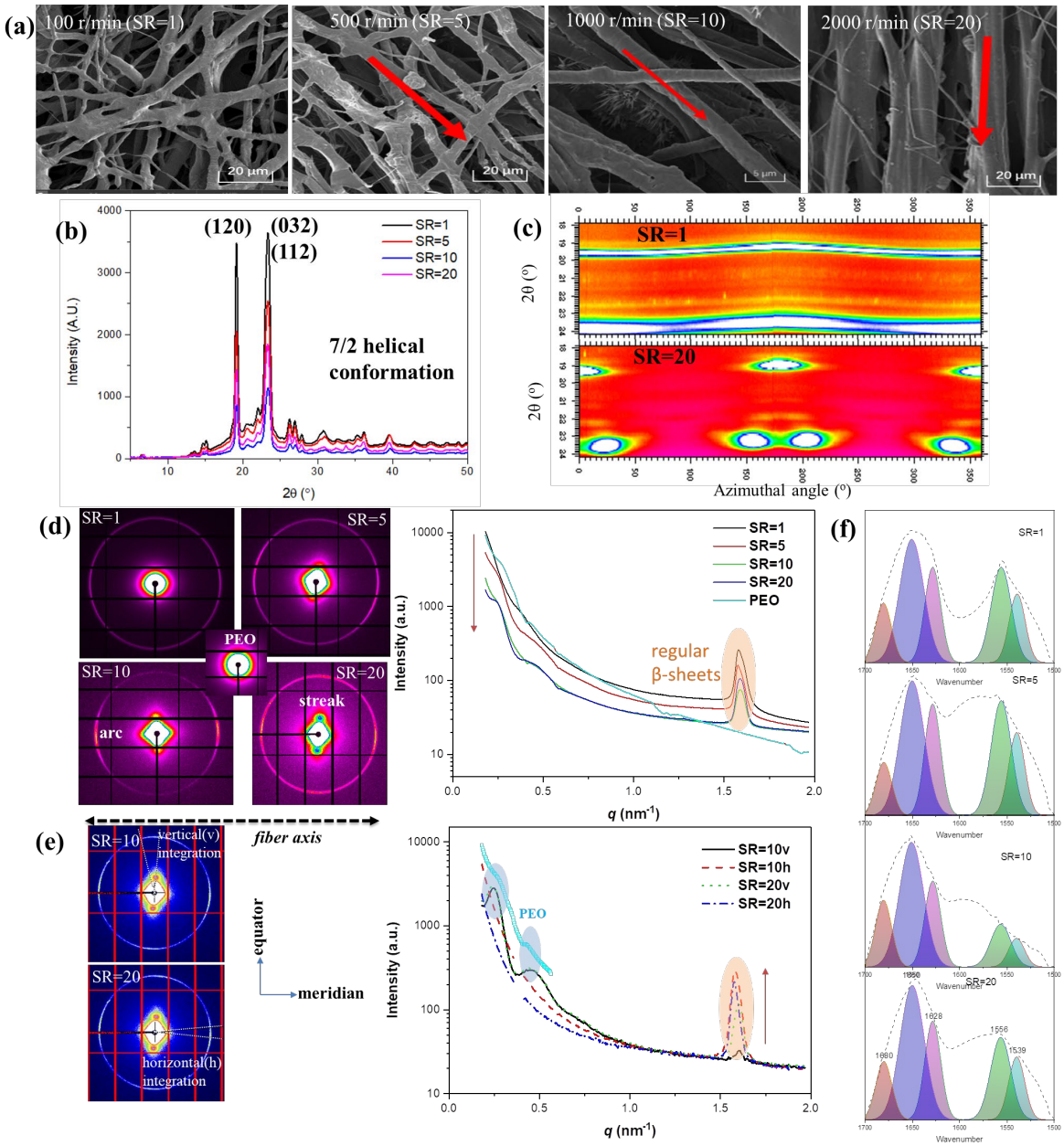

Figure 3. The stretching effect. (a) Microscopic fiber morphology by SEM imaging analysis, red arrows indicate fiber axis. (b) WXRD plots of the oriented fiber. (c) Azimuthal profile illustrating stretching effect on PEO crystal alignment. (d) Synchrotron 2D SAXS patterns together with their 1D integrated diffractograms. Concentrated arc, fiber streak and ordering configuration of polymer chains are highlighted. (e) Differences in polymer chains parallel or perpendicular to the fiber axis were found in samples with high stretching ratio (SR=10, SR=20).

(f) FTIR spectra deconvolution of the amide I and amide II bands within the stretched fiber samples.

Interestingly, differences in polymer chains parallel or perpendicular to the fiber axis were found in samples with high stretching ratios (SR=10 and 20), as shown in Figure 3e. Specifically, a cake integration in equator direction gives rise to three scattered peaks. The two shaded peaks at lower q values (<0.5 nm^{-1}) correspond to ordered packing of PEO polymer chains. The Bragg's long period (L_B) quantifying the average periodicity of lamellar stack (crystalline lamellae and inter-lamellar amorphous region) can be estimated from the Lorentz-corrected SAXS profile[52]. After Lorentz correction, the peak at q_{max} appears at 0.27 nm^{-1}, corresponding to L_B = 23.2 nm (Equation 1) for the standard sample (SR=1), which is in agreement with previously reported PEO average long period (25 nm) by SAXS analysis[53].

Previous studies demonstrated that stretching treatment were very likely to generate a fibrillation effect with low radius/height ratio of fibrils in oriented electrospun polymer fibers[49]. As a result, the average long period would increase slightly. For example, L_B of the stretched fiber mat (SR=10) was calculated as 26.1 nm, about 3 nm longer than that of the un-stretched mat (SR=1). Nevertheless, the calculation of exact length of fibril domain would require more complicated interpretation of SAXS patterns in terms of quantification of misorientation width, microvoids between fiber bundles, etc[54]. Besides, the following interesting phenomenon was observed during our study: a very high stretching force tends to deteriorate the orderly arrangement of microscopic crystal fibrils, generating misaligned fibril lamellae, as manifested by the appearance of isotropic halo pattern again for the highly stretched fiber mat (SR=20) like the one shown in the random fiber mat (SR=1), in contrast to the appearance of concentrated arcs

for the aligned fiber mat (SR=10) .

The meridional scattering intensity of the third peak (brown color shaded area) centered around 1.6 nm^{-1} is significantly higher than that of equatorial scattering. Since this peak is due to ordering configuration of protein chains (regular β-sheets explained in Figure 3d), clear comparison on these peak intensities suggests that the stretching treatment is highly likely to improve the fraction of ordered components of protein chains, like β-sheets, perpendicular to the fiber axis. FTIR spectra deconvolution analysis found further evidence on the stretch-improving share % of ordered β-sheet (Figure 3f). For instance, the estimated percentage of β-sheet nanocrystals is 30.4% for CPI/PEO-2000 (SR=20) versus 25.3% for CPI/PEO-100 (SR=1), see Table S3 (Supporting Information). The stretching effects on these structural transformations/ordering configurations are schematically illustrated in Figure 4.

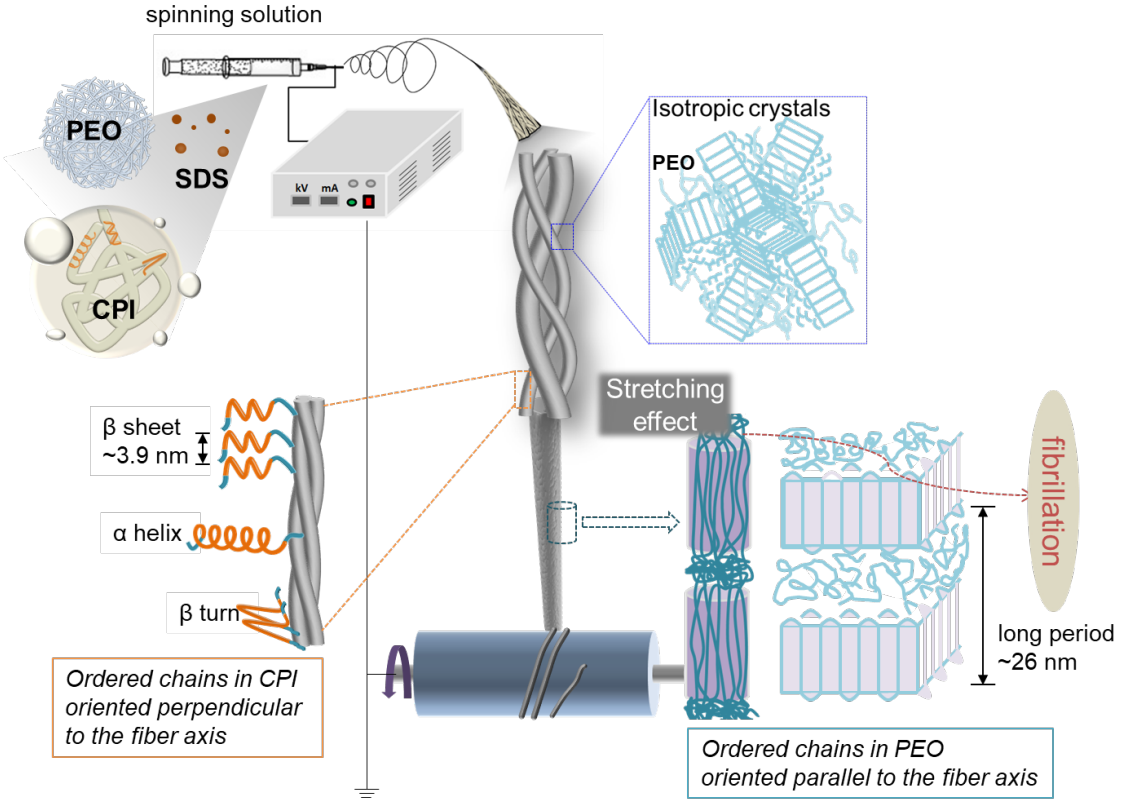

Figure 4. Schematic illustration of macromolecular chain entanglements during electrospinning and the stretching effects on transformation/ordering configurations of polymer chains.

The role of cross-linking

The impact of cross-linking on CPI/PEO fiber morphology and lyophobic properties were evaluated. Figure 5a shows that the CPI/PEO fibers become more uniform in the presence of the cross-linking agent ELO. With the increase of ELO content, the diameter of the electrospun fibers gradually increases, from 2.4 μm on average for CPI/PEO/ELO-0, to 4.4 μm for CPI/PEO/ELO-30. In addition, the treated fiber surfaces are much smoother than those of CPI/PEO fiber without ELO. However, when the addition of ELO content increases to 30%, the fiber bonded together, displaying a compact structure with reduced porosity. ELO molecules participate in the cross-linking reaction (Figure 2c,d and Figure S4, Supporting Information) and can generate a gel effect. As the cross-linking gelation process leads to a significant increase in intermolecular interactions thus increasing viscosity (Figure S6, Supporting Information), the solvent cannot evaporate fully. This makes it challenging to maintain a stable ejected solution during electro-spinning[55]. Therefore, it is recommended to use an appropriate amount of cross-linking agent; in case of the CPI/PEO/ELO fibers, 20% ELO relative to CPI content is considered as the best configuration.

Liquid resistance performance of the composite fiber mat was investigated by contact angle measurements. Bar charts of static water contact angle (WCA) and photos of water droplets on the surface of each fiber mat are shown in Figure 5b. The WCA of the CPI/PEO sample is only 31.5°, due to the presence of large numbers of hydroxyl and amino groups in protein and their strong interaction with water molecules[56]. However, the

WCA of the CPI/PEO/ELO fiber containing cross-linker ELO (10-30%) largely increased; specifically, averaged WCAs of CPC/SF/DAS10, CPC/SF/DAS20, and CPC/SF/DAS30 are 43°, 47°, and 64°, respectively, yet not being considered as hydrophobic surfaces (WCA>65°) [57]. Surprisingly, much higher contact angles were found in samples with higher ELO content (Figure 5c), irrespectively of probing liquids of varied properties like polarity and surface tension (water, ethylene glycol, glycerol and methylene iodide, Table S4, Supporting Information), displaying somewhat lyophobic effect. Cross-linked networks composed of tight polymer chains could naturally limit the transport and spread of liquid molecules when they penetrate into the fiber network[58].

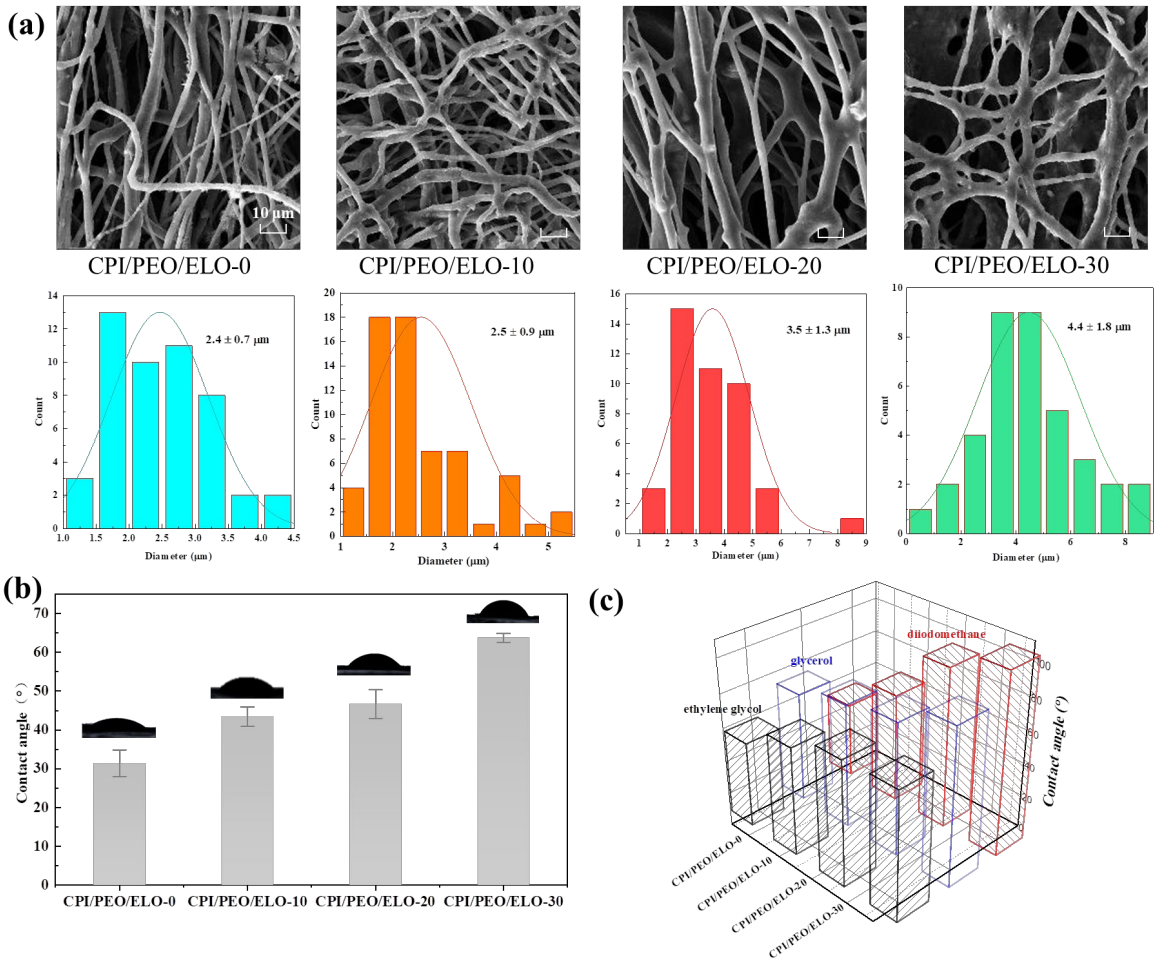

Figure 5. The effects of cross-linking on CPI/PEO fiber morphology and lyophobic properties. (a) SEM images of the crosslinked composite fiber samples CPI/PEO/ELO along with fiber diameter distribution. (b) Bar charts of static water contact angle and photos of water droplets on the fiber mat surfaces. (c) Lyophobic effect with high contact angles using liquids of varied properties like polarity and surface tension (water, ethylene glycol, glycerol and methylene iodide), especially evident for the crosslinked samples with higher ELO content.

Total surface energy (γ) of fiber samples was then estimated by the combination of dispersion component (γ_S^d) and polarity component (γ_S^p) of surface free energy, which were determined by Equation (5)[59] using glycerol and methylene iodide as probing liquid molecules.

$$\gamma_L(1 + cos\,\theta) = 2\left(\gamma_S^d \gamma_L^d\right)^{\frac{1}{2}} + 2\left(\gamma_S^p \gamma_L^p\right)^{\frac{1}{2}} \quad (5)$$

where θ, γ_L^d, and γ_L^p are the contact angle, dispersion and polarity components of liquid surface free energy respectively. Clearly, the ELO cross-linking treatments lead to much lower total surface energy (17.3 MJ/m^2 for CPI/PEO/ELO-30) compared to that of CPI/PEO/ELO-0 (49.9 MJ/m^2) and other similar biocomposite fibers[60], see details in Table 2. As previously discussed, the epoxy group of ELO would react with polar amino and carboxylic groups within the protein, consuming polar component of surface energy. Note that surface roughness, another key factor determining hydrophobicity[61] was not investigated here, as the prepared fiber mats are porous samples (Figure 5a) favoring liquid wetting and wicking phenomena[62].

Table 2 Contact angle (CA) and surface energy (γ) of CPI/PEO/ELO fibers

	CA	CA	CA	CA	γ^d	γ^p	γ

	(H_2O)	(ethylene glycol)	(glycerol)	(CH_2I_2)	(MJ/m^2)	(MJ/m^2)	(MJ/m^2)
CPI/PEO/ELO-0	31.5	51.2	45.6	66.3	0.88	49.0	49.9
CPI/PEO/ELO-10	43.4	64.7	65.9	74.3	3.45	25.9	29.4
CPI/PEO/ELO-20	46.7	74.1	95.7	79.1	24.2	0.67	24.8
CPI/PEO/ELO-30	63.7	75.2	107.4	92.5	17.1	0.19	17.3

Note: Total surface energy was determined by the combination of dispersion component and polarity component of surface free energy, using glycerol and methylene iodide as probing molecules.

Mechanical properties

The mechanical data presented in Figure 6 were taken from the CPI/PEO mats with fiber arrangement mainly in the direction of collector rotation (Machine direction), as illustrated in Figure 6a. Additional mechanical properties of the CPI/PEO mats in the direction perpendicular to the fiber axis (Transverse direction) were shown Figure S7, Supporting Information. The left hand side of Figure 6 shows the representative nominal stress and engineering strain curves as a function of the (a) CPI/PEO content, (b) the rotatory speed of the collector and (c) the content of crosslinking agent ELO. The right hand side of Figure 6 summarizes the maximum tensile strength (σ) and elongation at break (ε) values. Figure 6a compares the response of fiber mats manufactured at rotatory speed of 100 r/min and variable CPI/PEO content. All the fiber mats exhibit an elasto-plastic response with no distinct elastic limit, and final extensive plasticity. The smooth behavior of the stress-strain curves suggests crosslink failure of the fiber networks was negligible, thereby highlighting fiber rotation and plastic deformation as the primary

deformation mechanisms[63]. Overall, the gradual increment of CPI/PEO content increases the strength and elongation at break of the mats, with increments of the 114% in strength and 45.5% in elongation for the CPI/PEO-16 and CPI/PEO-14 mats respectively, when compare to the response of the baseline CPI/PEO-10 sample. The differences in mechanical response for each configuration correlate with the fiber diameter. Consequently, higher CPI/PEO content results in the creation of thicker fibers (Figure 1f), exhibiting superior mechanical properties in terms of strength and toughness.

Figure 6b compares the response of the fiber mats as a function of the rotatory speed of the collector. A progressive increase of stiffness and strength is evident as processing velocities rises, attributed to the greater load-bearing capacity of aligned fibers. The randomly oriented isotropic mat (collected speed of 100 r/min) exhibits the highest elongation to failure due to extensive fiber rotation and realignment towards the loading direction, delaying the final catastrophic fiber breakage. The stiffest and strongest response is obtained for 1000 r/min speed, with a significant increase of strength of 610%. Both configurations (100 and 1000 r/min) show similar toughness (area under the stress-strain curve, calculated as 1.63 kJ/m^3) which indicates a similar fiber molecular structure, in agreement with the SAXS observations (Figure 3d). The unidirectional fiber mat collected at 2000 r/min instead presented a weak mechanical response. This lower performance found in the highly stretched fiber mat (SR=20) could be associated with the less-ordered arrangement of crystal structure. If one observes 2D SAXS patterns in Figure 3d, the following interesting phenomenon can be found: Samples produced at SR=1, 5, 10 showed progressive differences in the external SAXS ring, which is the scattering of a diffraction plane aligned towards the fiber axis. Specifically, a halo diffraction in all

angles was seen for the randomly oriented fibers (SR=1), whereas fibers aligned towards a preferential direction (SR=10) displayed concentrated arcs only appearing perpendicular to the fiber. As for fiber mat spun at 2000 r/min, a halo ring diffraction in all angles appeared again, despite of its unidirectional alignment feature. At a very high collecting speed, macroscopic fiber bundles tend to align themselves; in the meantime, however, the high stretching force is likely to deteriorate the orderly arrangement of microscopic crystal structure, leading to misaligned lamellae as discussed above in SAXS data analysis.

Moreover, the ELO cross-linking treatment significantly improves the mechanical response of the mats in terms of strength and modulus (Figure 6c). The optimal ELO content, of 20wt% relative to CPI (CPI/PEO/ELO-20), provides an increment in strength of the 41% with respect to the baseline (no ELO) mat. The higher cross-linking density has a favorable effect by enhancing the load-bearing capacity through improved fiber connectivity. This leads to increased strength while causing a reduction in elongation at break[4] up to a 20 wt% ELO. The highest content of ELO addition (30 %wt) reduced the fiber strength, as a result of the unstabilities in the electrospinning process previously discussed. The brittle mechanical performance of CPI/PEO/ELO-30 might be ascribed to the presence of excessive ELO molecules just deposited on fiber surfaces that actually have no more chemical interactions with CPI (Figure S4, Supporting Information) and negligible load-bearing abilities[12]. Overall, the best mechanical properties in terms of balanced strength and toughness are achieved at an optimum spinning solution concentration (CPI/PEO-14), stretching ratio (1000 r/min, SR=10), and ELO content (CPI/PEO/ELO-20).

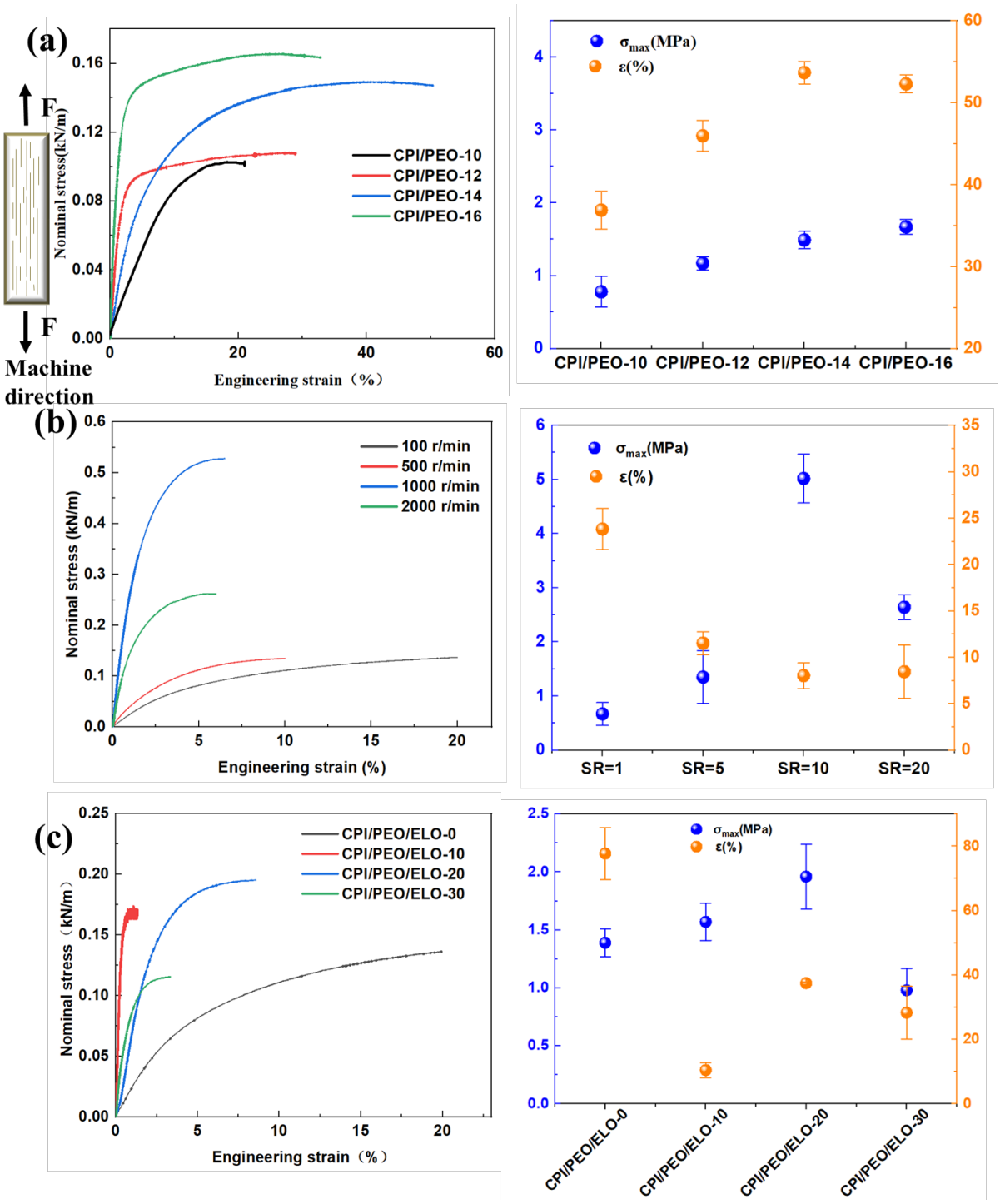

Figure 6. Plots of tensile nominal stress-engineering strain curves and corresponding tensile breaking strength and elongation at break. The composite fiber mat fabricated at different (a) spinning solution concentration, (b) fiber collecting rate, and (c) ELO addition content. Note that

6 repetitions were conducted for each sample and the average and standard deviation values were presented at the right.

Biocompatibility and water vapor permeability

For possible practical application in biomedical scaffolds or air filtration, cytotoxicity and water vapor permeability of the composite fiber mat were evaluated. The mouse kin fibroblast cells (L929) cultured onto the fiber samples were used for analyzing cytocompatibility, and the cell viability was determined by a CCK-8 detection kit. The control group with deionized water was also tested for comparison. As shown in Figure 7a, the cell viability for all samples was higher than 95%, regardless of stretching ratio (SR=1, 5, 10, 20) or cross-linking content (ELO 10%, 20%, 30%), suggesting a negligible toxicity to the skin cells [64]. Therefore, the fabricated fiber mats show a good biocompatibility with extremely low cytotoxicity.

Two samples with the highest stretching ratio and the greatest content of cross-linker were selected for water vapor permeability measurements, namely, the fiber mat CPC/PEO-2000 and CPC/PEO/ELO-30, respectively. The control sample CPC/PEO-100 produced with the lowest spinning speed and without cross-linker addition was also tested for comparison, shown in Figure 7b. The value of WVP for the highly stretched sample is 18% lower than that of the control. As shown previously the stretching orientation effect on CPI/PEO fiber morphology (Figure 3a), an orderly arrangement with increased fiber orientation was detected in fibers with higher SR values. More tightly and orderly arranged fibers are likely to generate a barrier and leave less free space for external water molecules to transport, thus giving rise to a lower value of WVP. When the fiber morphology variation is considered (Figure 5a), the cross-linked fiber mat

CPI/PEO/ELO-30 display higher diameter, smoother surface, and more connected structure with reduced porosity, pore volume (Figure S3, Supporting Information) and low surface area (Figure S2, Supporting Information); therefore, a lower value ($4.88 \pm 0.05 \times 10^{-9}$ $g \cdot m^{-1} \cdot s^{-1} \cdot Pa^{-1}$) with better barrier ability is expected as compared to the control.

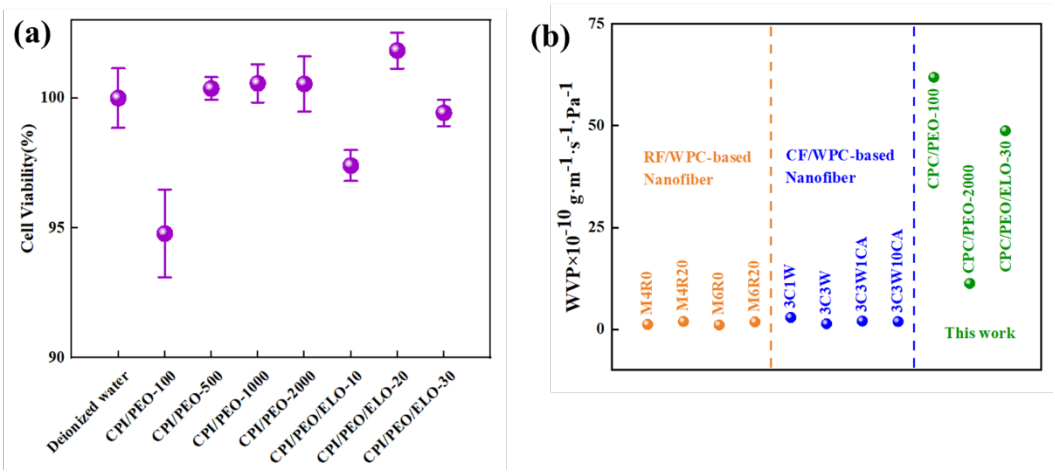

Figure 7. Fiber biocompatibility and water vapor permeability. (a) The cell viability of all samples (higher than 95%) determined by a CCK-8 detection kit suggests a negligible toxicity to the mouse kin fibroblast cells. In some cases, error-bar data more than 100% of cell viability are within experimental errors. (b) Water vapor permeability measurements of the stretched composite fiber mat CPC/PEO-2000 and the cross-linked fiber mat CPC/PEO/ELO-30, with the control sample CPC/PEO-100 (also without ELO) included for comparison.

Note that amino acid composition of the protein raw material used for fiber mat production also play a role in affecting WVP, in that hydrophilic amino acid groups could form more hydrogen bonds with water vapor molecules, leading to a bit higher WVP values. Conversely, the fiber mat made from the plant protein that contains higher amount of hydrophobic amino acids might have better water permeability. For instance, whey

protein contains more hydrophobic amino acids than cottonseed protein used in this study (Supplementary materials in Table S5 and Figure S8, Supporting Information). Indeed, WVP of two similar composite fiber mat materials (rye flour-whey protein-PEO and carob flour-whey protein-PEO) were found to be as low as $1.09\sim1.94\times10^{-10}$ $g\cdot m^{-1}\cdot s^{-1}\cdot Pa^{-1}$,[41] and $1.38\sim2.95\times10^{-10}$ $g\cdot m^{-1}\cdot s^{-1}\cdot Pa^{-1}$,[65] respectively.

Thermal properties

The thermal properties of the biocomposite fiber mats were investigated by DSC and TGA measurements, and the results are shown in Figure S9-S11 (Supporting Information). Cooling and heating ramp responses of all samples showed almost the same thermal characteristics. While crystallization during cooling was found at around 45 °C, a melting peak upon heating was centered at around 65 °C. These thermal transitions are due to the crystallization and melting of PEO crystals, suggesting clear phase segregation in the CPI/PEO composite where PEO polymer chains can crystallize without hindrances. However, the interactions between CPI and PEO polymer chains are evident if one compares enthalpy values (Table S6, Supporting Information) for crystallizing and melting process. As the spinning solution concentration increases, the enthalpies decrease noticeably. This observation may be justified by the presence of regions with more CPI and PEO chain entanglement/interaction, reducing the total PEO crystallinity. The same tendency of enthalpy change was observed in terms of the increase of CPI/PEO ratio (Table S6, Supporting Information). Moreover, when small amount of the crosslinker ELO was added to CPI/PEO composite, the formation of cross-linked networks may lower crystallization/melting energies, which is corroborated by the observation of lower

crystallization rate, as shown by isothermal crystallization behavior at 52 °C in Figure S10 (Supporting Information).

No important variations in TGA profiles (Figure S11, Supporting Information) were found for all fiber mats, reaffirming the fact that both polymers (CPI and PEO) are mostly segregated, having no influences on thermal degradation of the individual polymers. In summary, thermal analysis suggests that most PEO polymer chains in CPI/PEO composite fiber mats behave independently to thermal responses. CPI protein macromolecules, however, can partially interact with PEO polymer in terms of hydrogen bonding[20], which could promote chain entanglement, increase viscosity of spinning solution, and form condensed PCI/PEO electrospun fiber mats. This improvement of protein spinnability has been supported by previously shown evidences of the fiber mat morphology (Figure 1) and their structure analysis (Figure 2).

Conclusions

This study presents a methodology to obtain fiber mats from a sustainable source of oilseed protein (cottonseed) and reports a systematic nano and microscale characterisation of material properties at fundamental molecular level as a function of a diversity of processing parameters. In summary, cottonseed protein isolate was extracted from cottonseed powder waste, and blended with polyethylene oxide, and a small amount of surfactant sodium lauryl sulfate to create a spinnable fiber solution. CPI/PEO composite fiber mats with uniform and smooth fiber morphology were obtained with spinning solution concentration varying from 8 to 16wt%, and CPI/PEO ratio 1:9 to 4:6. Mechanical properties in terms of stiffness and strength could be tailored by modifying the rotatory speed of the collector. WAXD results suggest that orderly arrangement of

fiber mat and a preferential fiber alignment exist in mats with higher stretching ratio values. Synchrotron SAXS data indicate that average long period of PEO lamellar stack increase slightly due to a stretch-induced fibrillation effect; both SAXS and FTIR spectra deconvolution analysis suggest that stretching treatment can improve the fraction of ordered β-sheet components of protein chains.

In addition, the cross-linking agent significantly improves the tensile strength, water resistance, thermal stability, and solvent resistance of the fiber mats. For instance, the fiber mat containing 20% ELO showed good strength (1.96 MPa), low surface free energy (24.8 MJ/m^2), and superior solvent resistance (95.7°), compared with the fiber mat without ELO (1.35 MPa, 49.9 MJ/m^2 and 45.6°). Furthermore, the CCK-8 method testing mouse skin fibroblasts L929 suggests that the cytotoxicity of the composite fiber mats was extremely low, with cell viability>97%, showing good biocompatibility. The future large-scale fabrication of these biocompatible, lyophobic, aligned or cross-linked protein-derived fiber mats would have great potential in practical applications such as air filtration, biodegradable packaging, and water treatment.

Future interesting works of including bioactive substances with antibacterial, antifungal or anticancer activity in the spinning solution are worth of further study for biomedical dressing or tissue engineering. For example, the incorporation of bioactive glass into soy protein based nanofibrous scaffolds could support cell proliferation[66]; the addition of living cells into polycaprolactone fiber mat for liver implant tissue engineering[67]. Nevertheless, potentially high chemical reactivity of the cross-linking agent with bioactive agents might increase risks of consuming reactive groups of bioactive substances and losing bioactivity of the added drugs.

Supporting Information

The Supporting Information is available free of charge at http:// pubs.acs.org.

Experiments describing CPI extraction, protein content and molecular weight, BET test results, rheological parameters, percentage of protein secondary structure, background experiments on 2D WAXD scans, surface energy, amino acids, DSC and TGA thermal properties.

Author Information

*Corresponding Author

Hangbo Yue - Guangdong Provincial Key Laboratory of Plant Resources Biorefinery, School of Chemical Engineering & Light Industry, Guangdong University of Technology, Guangzhou 510006, China. E-mail:

E-mail: Hangbo Yue (hangbo.yue@gdut.edu.cn)

Notes

The authors declare no competing financial interest.

Acknowledgements

The authors would like to thank financial support from National Natural Science Foundation of China (22378078), Science and Technology Planning Project of Guangdong Province (No. 2023A0505050163), and Natural Science Foundation of Guangdong Province (2022A1515011500). Synchrotron SAXS experiments were performed at beamline BL16B1 at Shanghai Synchrotron Radiation Facility with the collaboration of beamline staff. Mr. L. Mai and Mr. X. Li are appreciated for help with contact angle measurements.

References

(1) Kuemmerer, K.; Clark, J. H.; Zuin, V. G. Rethinking chemistry for a circular economy. *Science* **2020**, *367* (6476), 369-370.
(2) Sheldon, R. A. Green chemistry and resource efficiency: towards a green economy. *Green Chem.* **2016**, *18* (11), 3180-3183.
(3) Tansaz, S.; Boccaccini, A. R. Biomedical applications of soy protein: A brief overview. *J. Biomed. Mater. Res. Part A* **2016**, *104* (2), 553-569.

(4) Liao, X.; Dulle, M.; de Souza e Silva, J. M.; Wehrspohn, R. B.; Agarwal, S.; Förster, S.; Hou, H.; Smith, P.; Greiner, A. High strength in combination with high toughness in robust and sustainable polymeric materials. *Science* **2019**, *366* (6471), 1376-1379.
(5) Mirpoor, S. F.; Giosafatto, C. V. L.; Porta, R. Biorefining of seed oil cakes as industrial co-streams for production of innovative bioplastics. A review. *Trends in Food Science & Technology* **2021**, *109*, 259-270.
(6) Yue, H.; Mai, L.; Xu, C.; Yang, C.; Shuttleworth, P. S.; Cui, Y. Recent advancement in bio-based adhesives derived from plant proteins for plywood application: A review. *Sustainable Chem. Pharm.* **2023**, *33*, 101143.
(7) Yang, Q.; Guo, J.; Liu, Y.; Guan, F.; Song, J.; Gong, X. Improved Properties of Cellulose/Antarctic Krill Protein Composite Fibers with a Multiple Cross-Linking Network. *Adv. Fiber Mater.* **2022**, *4* (2), 256-267.
(8) Lan, X.; Zhang, X.; Wang, L.; Wang, H.; Hu, Z.; Ju, X.; Yuan, Y. A review of food preservation based on zein: The perspective from application types of coating and film. *Food Chem.* **2023**, *424*, 136403.
(9) Luck, P. J.; Vardhanabhuti, B.; Yong, Y. H.; Laundon, T.; Barbano, D. M.; Foegeding, E. A. Comparison of functional properties of 34% and 80% whey protein and milk serum protein concentrates. *J. Dairy Sci.* **2013**, *96* (9), 5522-5531.
(10) Yue, H. B.; Cui, Y. D.; Shuttleworth, P. S.; Clark, J. H. Preparation and characterisation of bioplastics made from cottonseed protein. *Green Chem.* **2012**, *14* (7), 2009-2016.
(11) Selling, G. W.; Hojilla-Evangelista, M. P.; Hay, W. T.; Utt, K. D.; Grose, G. D. Preparation and properties of solution cast films from pilot-scale cottonseed protein isolate. *Ind. Crops Prod.* **2022**, *178*, 114615.
(12) Yue, H.; Zheng, Y.; Zheng, P.; Guo, J. W.; Fernandez, J. P.; Clark, J.; Cui, Y. On the improvement of properties of bioplastic composites derived from wasted cottonseed protein by rational cross-linking and natural fiber reinforcement. *Green Chem.* **2020**, *22*, 8642-8655, 10.1039/D0GC03245J.
(13) Li, L.; Yue, H.; Wu, Q.; Fernández-Blázquez, J. P.; Shuttleworth, P. S.; Clark, J. H.; Guo, J. Unveiling the reinforcement effects in cottonseed protein/polycaprolactone blend biocomposites. *Compos. Sci. Technol.* **2022**, *225*, 109480.
(14) Li, J.; Pradyawong, S.; Sun, X. S.; Wang, D.; He, Z.; Zhong, J.; Cheng, H. N. Improving adhesion performance of cottonseed protein by the synergy of phosphoric acid and water soluble calcium salts. *Int. J. Adhes. Adhes.* **2021**, *108*, 102867.
(15) Yue, H.; Xu, C.; Yao, J.; He, M.; Yin, G.; Cui, Y.; Yang, C.; Guo, J. Characterization and properties of plywood bioadhesive derived from cottonseed protein and sawdust cellulose. *Cellulose* **2022**, *29*, 5869-5881.
(16) Li, J.; Pradyawong, S.; He, Z.; Sun, X. S.; Wang, D.; Cheng, H. N.; Zhong, J. Assessment and application of phosphorus/calcium-cottonseed protein adhesive for plywood production. *J. Cleaner Prod.* **2019**, *229*, 454-462.
(17) Cheng, H. N.; Kilgore, K.; Ford, C.; Fortier, C.; Dowd, M. K.; He, Z. Cottonseed protein-based wood adhesive reinforced with nanocellulose. *J. Adhes. Sci. Technol.* **2019**, *33* (12), 1357-1368.
(18) Li, C.; Wu, J.; Shi, H.; Xia, Z.; Sahoo, J. K.; Yeo, J.; Kaplan, D. L. Fiber-Based Biopolymer Processing as a Route toward Sustainability. *Adv. Mater.* **2022**, *34* (1), 2105196, https://doi.org/10.1002/adma.202105196.

(19) Wang, Y.; Khan, M. A.; Chen, K.; Zhang, L.; Chen, X. Electrospinning of Natural Biopolymers for Innovative Food Applications: A Review. *Food Bioprocess Technol.* **2023**, *16* (4), 704-725.
(20) Qasim, S. B.; Najeeb, S.; Delaine-Smith, R. M.; Rawlinson, A.; Ur Rehman, I. Potential of electrospun chitosan fibers as a surface layer in functionally graded GTR membrane for periodontal regeneration. *Dent. Mater.* **2017**, *33* (1), 71-83.
(21) Vega-Lugo, A. C.; Lim, L. T. Electrospinning of Soy Protein Isolate Nanofibers. *J. Biobased Mater. Bioenergy* **2008**, *2* (3), 223-230.
(22) Budurova, D.; Ublekov, F.; Penchev, H. The use of formic acid as a common solvent for electrospinning of hybrid PHB/Soy protein fibers. *Mater. Lett.* **2021**, *301*, 130313.
(23) Popov Pereira da Cunha, M. D.; Aldana, A. A.; Abraham, G. A. Photo-crosslinked soy protein-based electrospun scaffolds. *Mater. Lett.: X* **2021**, *12*, 100115.
(24) Deng, A.; Yang, Y.; Du, S.; Yang, S. Electrospinning of in situ crosslinked recombinant human collagen peptide/chitosan nanofibers for wound healing. *Biomater. Sci.* **2018**, *6* (8), 2197-2208.
(25) Sahoo, S. K.; Khandelwal, V.; Manik, G. Influence of epoxidized linseed oil and sisal fibers on structure-property relationship of epoxy biocomposite. *Polym. Compos.* **2018**, *39* (S4), E2595-E2605.
(26) Dinu, R.; Briand, N.; Mija, A. Influence of Keratin on Epoxidized Linseed Oil Curing and Thermoset Performances. *ACS Sustainable Chem. Eng.* **2021**, *9* (46), 15641-15652.
(27) Gao, Y.; Bate, T. S. R.; Callanan, A. A Unification of Nanotopography and Extracellular Matrix in Electrospun Scaffolds for Bioengineered Hepatic Models. *ACS Appl. Bio Mater.* **2023**, *6* (6), 2158-2171.
(28) He, Z.; Zhang, H.; Olk, D. C. Chemical Composition of Defatted Cottonseed and Soy Meal Products. *PLoS One* **2015**, *10* (6), e0129933.
(29) Hammersley, A. FIT2D: a multi-purpose data reduction, analysis and visualization program. *J. Appl. Crystallogr.* **2016**, *49* (2), 646-652.
(30) Cser, F. About the Lorentz correction used in the interpretation of small angle X-ray scattering data of semicrystalline polymers. *J. Appl. Polym. Sci.* **2001**, *80* (12), 2300-2308.
(31) Kchaou, H.; Benbettaïeb, N.; Jridi, M.; Abdelhedi, O.; Karbowiak, T.; Brachais, C.-H.; Léonard, M.-L.; Debeaufort, F.; Nasri, M. Enhancement of structural, functional and antioxidant properties of fish gelatin films using Maillard reactions. *Food Hydrocolloids* **2018**, *83*, 326-339.
(32) Yue, H.; Rubalcaba, J. C.; Cui, Y.; Fernández-Blázquez, J. P.; Yang, C.; Shuttleworth, P. S. Determination of cross-sectional area of natural plant fibres and fibre failure analysis by in situ SEM observation during microtensile tests. *Cellulose* **2019**, *26* (8), 4693-4706.
(33) Accoroni, C.; Godoy, E.; Reinheimer, M. A. Performance evaluation of protein recovery from Argentinian soybean extruded-expelled meals under different operating conditions. *J. Food Eng.* **2020**, *274*, 109849.
(34) Chen, J.; Liu, G.; Pantalone, V.; Zhong, Q. Physicochemical properties of proteins extracted from four new Tennessee soybean lines. *J. Agric. Food Res.* **2020**, *2*, 100022.
(35) Farkas, B.; Balogh, A.; Cselkó, R.; Molnár, K.; Farkas, A.; Borbás, E.; Marosi, G.; Nagy, Z. K. Corona alternating current electrospinning: A combined approach for increasing the productivity of electrospinning. *Int. J. Pharm.* **2019**, *561*, 219-227.
(36) Myers, D. Polymeric Surfactants and Surfactant–Polymer Interactions. In *Surfactant Science and Technology*, 2005; pp 220-244.

(37) Lefebvre-Cases, E.; La Fuente, B. T. D.; Cuq, J. L. Effect of SDS on Casein Micelles: SDS-Induced Milk Gel Formation. *J. Food Sci.* **2001**, *66* (1), 38-42.
(38) Barnes, H. A.; Hutton, J. F.; Walters, K. *An Introduction to Rheology*; Elsevier, 1989. DOI: 10.1016/B978-0-444-87469-6.50006-8.
(39) Mirzaie Yegane, M.; Hashemi, F.; Vercauteren, F.; Meulendijks, N.; Gharbi, R.; Boukany, P. E.; Zitha, P. Rheological response of a modified polyacrylamide–silica nanoparticles hybrid at high salinity and temperature. *Soft Matter* **2020**, *16* (44), 10198-10210, 10.1039/D0SM01254H.
(40) Suganya Bharathi, B.; Stalin, T. Cerium oxide and peppermint oil loaded polyethylene oxide/graphene oxide electrospun nanofibrous mats as antibacterial wound dressings. *Mater. Today Commun.* **2019**, *21*, 100664.
(41) Aslaner, G.; Sumnu, G.; Sahin, S. Encapsulation of Grape Seed Extract in Rye Flour and Whey Protein–Based Electrospun Nanofibers. *Food Bioprocess Technol.* **2021**, *14* (6), 1118-1131.
(42) Yang, H.; Yang, S.; Kong, J.; Dong, A.; Yu, S. Obtaining information about protein secondary structures in aqueous solution using Fourier transform IR spectroscopy. *Nat. Protoc.* **2015**, *10* (3), 382-396.
(43) Krimm, S.; Bandekar, J. Vibrational spectroscopy and conformation of peptides, polypeptides, and proteins. *Advance in Protein Chemistry* **1986**, *38*, 181-364.
(44) Byler, D. M.; Susi, H. Examination of the secondary structure of proteins by deconvolved FTIR spectra. *Biopolymers* **1986**, *25* (3), 469-487.
(45) Sharma, B. K.; Liu, Z.; Adhvaryu, A.; Erhan, S. Z. One-Pot Synthesis of Chemically Modified Vegetable Oils. *J. Agric. Food. Chem.* **2008**, *56* (9), 3049-3056.
(46) Altuna, F. I.; Pettarin, V.; Williams, R. J. J. Self-healable polymer networks based on the cross-linking of epoxidised soybean oil by an aqueous citric acid solution. *Green Chem.* **2013**, *15* (12), 3360-3366, 10.1039/C3GC41384E.
(47) Kakade, M. V.; Givens, S.; Gardner, K.; Lee, K. H.; Chase, D. B.; Rabolt, J. F. Electric Field Induced Orientation of Polymer Chains in Macroscopically Aligned Electrospun Polymer Nanofibers. *J. Am. Chem. Soc.* **2007**, *129* (10), 2777-2782.
(48) Pakravan, M.; Heuzey, M. C.; Ajji, A. Core-shell structured PEO-chitosan nanofibers by coaxial electrospinning. *Biomacromolecules* **2012**, *13* (2), 412-421.
(49) Gazzano, M.; Gualandi, C.; Zucchelli, A.; Sui, T.; Korsunsky, A. M.; Reinhard, C.; Focarete, M. L. Structure-morphology correlation in electrospun fibers of semicrystalline polymers by simultaneous synchrotron SAXS-WAXD. *Polymer* **2015**, *63*, 154-163.
(50) Fitzpatrick, A. W.; Debelouchina, G. T.; Bayro, M. J.; Clare, D. K.; Caporini, M. A.; Bajaj, V. S.; Jaroniec, C. P.; Wang, L.; Ladizhansky, V.; Muller, S. A.; et al. Atomic structure and hierarchical assembly of a cross-beta amyloid fibril. *Proc Natl Acad Sci U S A* **2013**, *110* (14), 5468-5473.
(51) Drummy, L. F.; Farmer, B. L.; Naik, R. R. Correlation of the beta-sheet crystal size in silk fibers with the protein amino acid sequence. *Soft Matter* **2007**, *3* (7), 877-882.
(52) Alvaredo, Á.; Martín, M. I.; Castell, P.; Guzmán de Villoria, R.; Fernández-Blázquez, J. P. Non-Isothermal Crystallization Behavior of PEEK/Graphene Nanoplatelets Composites from Melt and Glass States. *Polymers* **2019**, *11* (1), 124.
(53) Lisowski, M. S.; Liu, Q.; Cho, J.; Runt, J.; Yeh, F.; Hsiao, B. S. Crystallization Behavior of Poly(ethylene oxide) and Its Blends Using Time-Resolved Wide- and Small-Angle X-ray Scattering. *Macromolecules* **2000**, *33* (13), 4842-4849.

(54) Ruland, W. Small-angle scattering studies on carbonized cellulose fibers. *Journal of Polymer Science Part C: Polymer Symposia* **1969**, *28* (1), 143-151.
(55) Xue, J.; Wu, T.; Dai, Y.; Xia, Y. Electrospinning and Electrospun Nanofibers: Methods, Materials, and Applications. *Chem. Rev.* **2019**, *119* (8), 5298-5415.
(56) Martín-Alfonso, J. E.; Félix, M.; Romero, A.; Guerrero, A. Development of new albumen based biocomposites formulations by injection moulding using chitosan as physicochemical modifier additive. *Composites, Part B* **2014**, *61*, 275-281.
(57) Vogler, E. A. Structure and reactivity of water at biomaterial surfaces. *Adv. Colloid Interface Sci.* **1998**, *74* (1), 69-117.
(58) Yue, H.; Fernández-Blázquez, J.; Shuttleworth, P.; Cui, Y. D.; Ellis, G. Thermomechanical relaxation and different water states in cottonseed protein derived bioplastics. *RSC Adv.* **2014**, *4* (61), 32320-32326.
(59) Owens, D. K.; Wendt, R. C. Estimation of the surface free energy of polymers. *J. Appl. Polym. Sci.* **1969**, *13* (8), 1741-1747, https://doi.org/10.1002/app.1969.070130815.
(60) Jirkovec, R.; Erben, J.; Sajdl, P.; Chaloupek, J.; Chvojka, J. The effect of material and process parameters on the surface energy of polycaprolactone fibre layers. *Mater. Des.* **2021**, *205*, 109748.
(61) Liu, M.; Wang, S.; Jiang, L. Nature-inspired superwettability systems. *Nat. Rev. Mater.* **2017**, *2* (7), 17036.
(62) deGennes, P.-G.; Brochard-Wyart, F.; Quéré, D. *Capillarity and Wetting Phenomena: Drops, Bubbles, Pearls, Waves*; Springer 2004. DOI: https://doi.org/10.1007/978-0-387-21656-0.
(63) Camarena-Maese, F. J.; Martínez-Hergueta, F.; Fernández-Blázquez, J. P.; Kok, R. W.; Reid, J.; Callanan, A. Multiscale SAXS/WAXD characterisation of the deformation mechanisms of electrospun PCL scaffolds. *Polymer* **2020**, *203*, 122775.
(64) Hu, L.; Zhong, Y.; Wu, S.; Wei, P.; Huang, J.; Xu, D.; Zhang, L.; Ye, Q.; Cai, J. Biocompatible and biodegradable super-toughness regenerated cellulose via water molecule-assisted molding. *Chem. Eng. J.* **2021**, *417*, 129229.
(65) Zeren, S.; Sahin, S.; Sumnu, G. Encapsulation of Caffeic Acid in Carob Bean Flour and Whey Protein-Based Nanofibers via Electrospinning. *Foods* **2022**, *11* (13), 1860.
(66) Tansaz, S.; Liverani, L.; Vester, L.; Boccaccini, A. R. Soy protein meets bioactive glass: Electrospun composite fibers for tissue engineering applications. *Mater. Lett.* **2017**, *199*, 143-146.
(67) Gao, Y. X.; Bate, T. S. R.; Callanan, A. A Unification of Nanotopography and Extracellular Matrix in Electrospun Scaffolds for Bioengineered Hepatic Models. *ACS Appl. Bio Mater.* **2023**, *6* (6), 2158-2171.